

See discussions, stats, and author profiles for this publication at: <https://www.researchgate.net/publication/289541962>

# Sensor-Specific Error Statistics for SST in the Advanced Clear-Sky Processor for Oceans

ARTICLE in JOURNAL OF ATMOSPHERIC AND OCEANIC TECHNOLOGY · FEBRUARY 2016

Impact Factor: 1.73 · DOI: 10.1175/JTECH-D-15-0166.1

---

READS

10

## 4 AUTHORS, INCLUDING:



**B. Petrenko**

National Oceanic and Atmospheric Adminis...

**55** PUBLICATIONS **91** CITATIONS

[SEE PROFILE](#)



**Yury Kihai**

National Oceanic and Atmospheric Adminis...

**35** PUBLICATIONS **99** CITATIONS

[SEE PROFILE](#)



**Prasanjit Dash**

National Oceanic and Atmospheric Adminis...

**46** PUBLICATIONS **470** CITATIONS

[SEE PROFILE](#)



# AMERICAN METEOROLOGICAL SOCIETY

*Journal of Atmospheric and Oceanic Technology*

## **EARLY ONLINE RELEASE**

This is a preliminary PDF of the author-produced manuscript that has been peer-reviewed and accepted for publication. Since it is being posted so soon after acceptance, it has not yet been copyedited, formatted, or processed by AMS Publications. This preliminary version of the manuscript may be downloaded, distributed, and cited, but please be aware that there will be visual differences and possibly some content differences between this version and the final published version.

The DOI for this manuscript is doi: 10.1175/JTECH-D-15-0166.1

The final published version of this manuscript will replace the preliminary version at the above DOI once it is available.

If you would like to cite this EOR in a separate work, please use the following full citation:

Petrenko, B., A. Ignatov, Y. Kihai, and P. Dash, 2016: Sensor-Specific Error Statistics for SST in the Advanced Clear-Sky Processor for Oceans. *J. Atmos. Oceanic Technol.* doi:10.1175/JTECH-D-15-0166.1, in press.



# Sensor-Specific Error Statistics for SST in the Advanced Clear-Sky Processor for Oceans

B. Petrenko<sup>1,2</sup>, A. Ignatov<sup>1</sup>, Y. Kihai<sup>1,2</sup>, P. Dash<sup>1,3</sup>

<sup>1</sup>NOAA STAR, <sup>2</sup>GST, Inc., <sup>3</sup>CIRA

---

Corresponding author address and e-mail:

Boris Petrenko, 5830 University Research Court, College Park, MD, 20740

boris.petrenko@noaa.gov

19   **Abstract**

20   The formulation of the Sensor-Specific Error Statistics (SSES) has been redesigned in the  
21   latest implementation of the NOAA Advanced Clear-Sky Processor for Oceans (ACSPO) to  
22   enable efficient use of SSES for assimilation of the ACSPO baseline regression SST (BSST)  
23   into L4 analyses. The SSES algorithm employs segmentation of the SST domain in the space  
24   of regressors and derives the segmentation parameter from the statistics of regressors within  
25   the global dataset of matchups. For each segment, local regression coefficients and SDs of  
26   BSST minus *in situ* SST are calculated from the corresponding subset of matchups. The local  
27   regression coefficients are used to generate an auxiliary product - Piecewise Regression  
28   (PWR) SST, and SSES biases are estimated as differences between BSST and PWR SST.  
29   Correction of SSES biases, which transforms BSST back into PWR SST, reduces the effects  
30   of residual cloud, variations in view zenith angle and, during the daytime, diurnal surface  
31   warming. This results in significant reduction in the global SD of fitting *in situ* SST, making it  
32   comparable with SD for the Canadian Meteorological Centre (CMC) L4 SST. Unlike the  
33   foundation CMC SST (which is consistent with *in situ* SST at night, but biased cold during the  
34   daytime), the PWR SST is consistent with *in situ* data during both day and night and thus may  
35   be viewed as an estimate of “depth” *in situ* SST. The PWR SST is expected to be a useful  
36   input into L4 SST analyses, especially for foundation SST products such as the CMC L4.

## 37    **1. Introduction**

38    Sea surface temperature (SST; see Table 1 for the list of abbreviations used in this paper) is a  
39    key environmental variable, which is routinely retrieved from satellite observations and used  
40    in many applications. Several processing centers generate Level 2 (L2) SST products from  
41    infrared satellite sensors data. To facilitate data exchange and use, the international Group for  
42    High Resolution SST (GHRSST) has established the GHRSST Data Specification format  
43    (GDS 2.0, the description is available at [https://www.ghrsst.org/documents/q/category/ghrsst-](https://www.ghrsst.org/documents/q/category/ghrsst-data-processing-specification-gds/operational/)  
44    [data-processing-specification-gds/operational/](https://www.ghrsst.org/documents/q/category/ghrsst-data-processing-specification-gds/operational/)). One of the GDS 2.0 requirements is that  
45    Sensor-Specific Error Statistics (SSES), i.e. estimates of SST bias and standard deviation  
46    (SD), should be appended to each reported SST value. However, no specific guidance was  
47    provided on how the SSES should be calculated. As a result, different SSES definitions were  
48    implemented by EUMETSAT Ocean and Sea Ice Satellite Application Facility (OSI-SAF  
49    Low Earth Orbiter SST Product User Manual, 2009), NAVO ([Cayula et al. 2004](#)), NASA  
50    (Kilpatrick et al. 2015), and NOAA in the Advanced Clear-Sky Processor for Oceans  
51    (ACSPO) system (Petrenko and Ignatov 2014a). Although the SSES is specifically intended to  
52    facilitate blending of different satellite L2 and L3 products and their assimilation into L4  
53    analyses, the authors are not aware of any documented improvements in the data assimilation  
54    due to the use of any available SSES data. Consequently, the GHRSST-XV meeting in June  
55    2014 has reviewed existing SSES practices, and suggested revisiting those (Proceedings of  
56    GHRSST-XV, 2014).

57    In this context, the ACSPO SSES has been redesigned with the explicit objective to achieve a  
58    positive effect on the L4 analyses. Typically, assimilation of satellite SSTs involves correction  
59    of biases in satellite SST with respect to *in situ* SST (or with respect to a reference satellite

product) (e.g., [Reynolds et al. 2002](#); [Brasnett 2008](#); Donlon et al. 2012). Since many L4 products position themselves as “foundation” (defined at the depth below which no diurnal warming is present; Donlon et al. 2007) or “depth” (i.e., representative of *in situ* SSTs), our primary objective was achieving a measurable improvement in estimation of ACSPO SST biases with respect to *in situ* SST (and thus minimize the need for an empirical bias correction as an initial step of L4 processing). Another goal of the SSES redesign was redefining the SSES SDs to reflect more realistically the dependence of the retrieval errors on observational conditions. However, this paper focuses on the SSES biases and leaves the evaluation of SSES SDs for the future work.

As documented in ([Petrenko et al. 2014b](#)), the baseline ACSPO SSTs (BSST,  $T_S$ ) are produced with the regression equations proposed by Lavanant et al. (2012):

$$\text{Day: } T_S = a_0 + a_1 T_{11} + a_2 S_\theta T_{11} + a_3 \Delta T + a_4 T_s^0 \Delta T + a_5 S_\theta \Delta T + a_6 S_\theta \quad (1)$$

$$\text{Night: } T_S = b_0 + b_1 T_{3.7} + b_2 S_\theta T_{3.7} + b_3 \Delta T + b_4 S_\theta \Delta T + b_5 S_\theta \quad (2)$$

Here,  $T_{3.7}$ ,  $T_{11}$ , and  $T_{12}$  are brightness temperatures (BTs) observed at 3.7  $\mu\text{m}$ , 11  $\mu\text{m}$  and 12  $\mu\text{m}$  respectively;  $\Delta T = T_{11} - T_{12}$ ;  $S_\theta = \sec\theta - 1$ ;  $\theta$  is satellite view zenith angle (VZA);  $T_s^0$  is the “first guess” SST (in degrees Celsius) obtained by interpolation of gridded L4 SST to sensor’s pixels. Currently, ACSPO uses L4 SST by the Canadian Meteorological Centre (CMC) ([Brasnett 2008](#)). Both Eq. (1) and (2) are used in ACSPO with a single set of regression coefficients,  $a_i$ ,  $i=0,1,\dots,6$ , and  $b_i$ ,  $i=0,1,\dots,5$ , trained on a global dataset of matchups (MDS). Customarily, SST retrieval errors are estimated with respect to *in situ* SSTs. For regression algorithms, such as BSST, retrieval errors are largely caused by inaccuracy of global approximation of a highly variable inverse relationship between BTs and SST with a

82 single regression equation, and with a single set of coefficients. These errors essentially  
83 depend on the observational conditions, characterized by such variables as VZA, total  
84 precipitable water vapor content in the atmosphere (TPW), wind speed, proximity to clouds  
85 etc (e.g., Castro et al. 2008; Xu et al. 2009; Petrenko et al. 2014b).

86 In order to be realistic, the SSES should account for the dependence of BSST errors on  
87 observational conditions. This may be accomplished by separate estimation of SSES for the  
88 segments of the whole SST domain, which are relatively uniform in terms of retrieval errors.  
89 The initial ACSPO SSES algorithm (Petrenko and Ignatov 2014a) performed the  
90 segmentation of the SST domain in terms of VZA and TPW. This approach, however, was  
91 found inefficient because the real number of physical variables affecting the retrieval errors is  
92 not limited to these two variables. Some approaches suggested accounting for more physical  
93 variables (e.g., under-screened cloud, aerosols, wind speed, etc. (e.g., Castro et al. 2008; Xu et  
94 al. 2009; Minnett 2014; Griffin 2014). However, it remains unclear whether accounting for all  
95 physical factors essentially affecting retrieval errors is possible.

96 In the redesigned ACSPO SSES, a different approach is explored, in which the retrieval errors  
97 are considered as functions of regressors (i.e. terms on the right-hand side of the regression  
98 equations, excluding the offsets) rather than certain physical variables. This way, the  
99 variations in BSST can be explained with a limited number of arguments, no matter how  
100 many physical variables the regressors depend on. The criteria for segmentation of the SST  
101 domain in the space of regressors (**R**-space) are derived from the statistical distribution of  
102 regressors within the training MDS. During the algorithm training, these criteria are used to  
103 subdivide the global MDS into subsets of matchups belonging to specific segments. This  
104 allows calculation for each segment SSES SDs and local regression coefficients. At the stage

of the L2 production, the SSES SDs and the local coefficients are obtained from the LUT according to the regressors' values at each pixel. The local regression coefficients are used to create an auxiliary SST product - Piecewise Regression SST ( $T_{PWR}$ , PWR SST), and the SSES biases are calculated as difference between the BSST and PWR SST.

The theoretical basis for the segmentation of the SST domain in the  $\mathbf{R}$ -space is provided in Section 2. The implementation of the SSES algorithm in ACSPO version 2.4 is described in Section 3. The performance of the SSES bias correction is evaluated in Section 4. Section 5 summarizes and concludes.

## 2. Segmentation of the SST domain in the space of regressors

Each of Eq. (1) and (2) can be rewritten as follows:

$$T_S = \langle T_S^{is} \rangle + \mathbf{c}^T(\mathbf{R} - \langle \mathbf{R} \rangle) + \epsilon \quad (3)$$

Here,  $\mathbf{R}$  is a vector of regressors;  $T_S^{is}$  is *in situ* SST,  $\mathbf{c}$  is a vector of global coefficients,  $\langle * \rangle$  denotes averaging over the global training MDS and  $\epsilon$  is the error of regression approximation of  $T_S^{is}$ . The vector of coefficients is estimated with the least squares method (Bard 1974) assuming that  $\epsilon$  has a Gaussian distribution with a zero mean and SD = 1:

$$\mathbf{c} = \mathbf{D}^{-1} \langle (\mathbf{R} - \langle \mathbf{R} \rangle) (T_S^{is} - \langle T_S^{is} \rangle) \rangle, \quad (4)$$

$\mathbf{D}$  is a covariance matrix of regressors within the MDS:

$$\mathbf{D} = \langle (\mathbf{R} - \langle \mathbf{R} \rangle) (\mathbf{R} - \langle \mathbf{R} \rangle)^T \rangle. \quad (5)$$

The covariance matrix of the estimated vector of coefficients (4) is  $\mathbf{D}^{-1}$ . It follows from Eq. (3-5) that the SST estimate (3) is a function of a vector of regressors  $\mathbf{R}$  at a given pixel and the



125 statistics of regressors within the training MDS,  $\langle \mathbf{R} \rangle$  and  $\mathbf{D}$ . This suggests that the error  $\delta T_S$   
 126 of the SST estimate (3) should also be a function of these statistics. Differentiating Eq. (3) in  
 127 terms of  $\mathbf{c}$  gives a relationship between  $\delta T_S$  and the uncertainty  $\delta \mathbf{c}$  of the vector of  
 128 coefficients:

$$129 \quad \delta T_S = \delta \mathbf{c}^T (\mathbf{R} - \langle \mathbf{R} \rangle). \quad (6)$$

130 The variance of  $\delta T_S$  is estimated from Eq. (6) as follows:

$$131 \quad V(\delta T_S) = \rho^2, \quad (7)$$

$$132 \quad \rho = [(\mathbf{R} - \langle \mathbf{R} \rangle)^T \mathbf{D}^{-1} (\mathbf{R} - \langle \mathbf{R} \rangle)]^{0.5} \quad (8)$$

133 Parameter  $\rho$  can be viewed as a distance between  $\mathbf{R}$  and  $\langle \mathbf{R} \rangle$  in the  $\mathbf{R}$ -space. In the past, a  
 134 similar parameter derived from *a posteriori* distribution of retrieved variables was used in the  
 135 retrieval algorithms based on the inversion of the radiative transfer model. Kozlov (1966)  
 136 used it as a metric in the space of retrieved variables. Merchant et al. (2008) found that the  
 137 errors of the optimal SST estimation increase with  $\rho$ . Eq. (7) suggests that a similar  
 138 dependence takes place between the variance of the SST, estimated with Eq. (3), and the  $\rho$   
 139 derived from the distribution of regressors within the MDS. Following Kozlov (1966), we  
 140 refer to the  $\rho$  as the Fisher distance in the  $\mathbf{R}$ -space.

141 Eq. (7) was derived under the aforementioned assumptions regarding the error  $\varepsilon$  of the  
 142 baseline regression SST. In reality, the  $V(\delta T_S)$  may not be equal to  $\rho^2$ , but, as shown below in  
 143 Section 3, it remains a quasi-monotonic function of  $\rho$ . Therefore, a segmentation of the SST  
 144 domain in terms of  $\rho$  may be viewed as a proxy for segmentation in terms of  $V(\delta T_S)$ . Another  
 145 advantage of using  $\rho$  as a segmentation parameter follows from the fact that  $\rho$  is an argument

146 of the Gaussian approximation of the probability density function (PDF) of  $\mathbf{R}$  within the  
 147 training MDS. The standard expression for this PDF (Bury 1975) has the following form:

$$148 \quad P(\mathbf{R}) = [(2\pi)^N \det(\mathbf{D})]^{-0.5} \exp[-[(\mathbf{R} - \langle \mathbf{R} \rangle)^T \mathbf{D}^{-1} (\mathbf{R} - \langle \mathbf{R} \rangle)]/2], \quad (9)$$

149 Considering Eq. (8), Eq. (9) can be rewritten as follows:

$$150 \quad P(\mathbf{R}) = [(2\pi)^N \det(\mathbf{D})]^{-0.5} \exp[-\rho^2/2] \quad (10)$$

151 Here,  $N$  is the dimensionality of  $\mathbf{R}$ , i.e., the number of regressors from which the  $\mathbf{R}$ -space is  
 152 constructed. It follows from Eq. (10) that  $\rho$  characterizes the extent, to which a given vector of  
 153 regressors  $\mathbf{R}$  is represented in the training MDS. Given the PDF by Eq. (10),  $\rho^2$  has a  $\chi^2$  –  
 154 distribution with  $N$  degrees of freedom (Bury 1975). The PDF of the  $\chi^2$  – distribution has a  
 155 maximum at some small value of  $\rho$  and rapidly declines with increasing or decreasing  $\rho$ . This  
 156 simplifies the segmentation process by limiting the range of considered  $\rho$  values.

157 Note that whereas Eq. (7) characterizes the average dependence of  $V(\delta T_s)$  on  $\rho$  over all  
 158 directions in the  $\mathbf{R}$ -space, such dependencies may vary with specific directions. For example,  
 159 assuming that the mean vector  $\langle \mathbf{R} \rangle$  corresponds to some "mean" value of the atmospheric  
 160 absorption  $\tau$ , the non-linear dependencies of BTs on the  $\tau$  may result in different dependencies  
 161 of  $V(\delta T_s)$  on  $\rho$  along the opposite directions corresponding to decreasing and increasing  $\tau$ . To  
 162 account for the anisotropy of the retrieval errors in the  $\mathbf{R}$ -space, we introduce an orthogonal  
 163 basis consisting of  $N$  eigenvectors of the covariance matrix  $\mathbf{D}$  with the origin at  $\langle \mathbf{R} \rangle$  and  
 164 perform segmentation in terms of  $\rho$  separately in each of  $2^N$  orthants of this basis.

### 3. Implementation of SSES in ACSPO

The segmentation concept described in Section 2 is the foundation of the redesigned ACSPO SSES algorithm. For the daytime, the  $\mathbf{R}$ -space is constructed from the regressors of Eq. (1), i.e. the vector of regressors has the following six components:

$$\mathbf{R} = [T_{11}, S_{\theta}T_{11}, \Delta T_{11-12}, T_s^0 \Delta T_{11-12}, S_{\theta} \Delta T_{11-12}, S_{\theta}]^T \quad (11)$$

For the nighttime, however, it was found that the five regressors appearing in Eq. (2) are not sufficient to adequately capture the full range of observational conditions. Therefore, the set of  $\mathbf{R}$  components was extended and now includes the following 9 components:

$$\mathbf{R} = [T_{3.7}, S_{\theta}T_{3.7}, \Delta T_{11-12}, \Delta T_{3.7-12}, T_s^0 \Delta T_{11-12}, T_s^0 \Delta T_{3.7-12}, S_{\theta} \Delta T_{11-12}, S_{\theta} \Delta T_{3.7-12}, S_{\theta}]^T \quad (12)$$

Here,  $\Delta T_{3.7-12} = T_{3.7} - T_{12}$ .

The performance of the described SSES algorithm is explored in this paper using data from six satellite sensors: S-NPP VIIRS, Aqua and Terra MODISs, Metop-A and Metop-B AVHRRs (both in the Full Resolution Area Coverage, FRAC, mode with 1 km spatial resolution at nadir) and NOAA-19 AVHRR (in the Global Area Coverage, GAC, mode with 4 km spatial resolution at nadir), routinely processed at NOAA with ACSPO. For all these sensors, the global MDS were collected from 15 May 2013 to 8 August 2014 using clear-sky BTs selected with the ACSPO Clear-Sky Mask (Petrenko et al. 2010) and drifting and tropical moored buoys from the NOAA *in situ* Quality Monitor (iQuam; Xu and Ignatov 2014). The *in situ* SSTs were selected using the iQuam flag showing the suitability for high-accuracy applications (available at <http://www.star.nesdis.noaa.gov/sod/sst/iquam/data.html>). Every *in situ* SST was matched with the nearest clear-sky satellite pixel within the 10 km distance and the time period of  $\pm 2$  hours.

187 The MDS were used to calculate the statistics  $\langle \mathbf{R} \rangle$  and  $D$  both for day and night.

188 Table 2 shows the total numbers of matchups in the global MDSs for 6 satellite instruments,  
189 S-NPP VIIRS, Aqua and Terra MODISs, Metop-A and Metop-B AVHRRs (both in the Full  
190 Resolution Area Coverage, FRAC, mode with 1 km spatial resolution at nadir) and NOAA-19  
191 AVHRR (in the Global Area Coverage, GAC, mode with 4 km spatial resolution at nadir).

192 The basis in the  $\mathbf{R}$ -space with the origin at  $\langle \mathbf{R} \rangle$  was introduced as a set of eigenvectors of the  
193 covariance matrix  $D$ , and the Fisher distances were calculated for all matchups according to  
194 Eq. (8). Fig. 1 shows histograms of the matchups as functions of the Fisher distance for six  
195 sensors. Recall that the Fisher distance characterizes the extent, to which a given vector of  
196 regressors  $\mathbf{R}$  is typical within a given MDS, and, at the same time, represents a scaled  
197 variance of the retrieval error,  $V(\delta T_S)$ . The shape of the histograms is similar for all sensors:  
198 the majority of matchups are concentrated within a limited range of  $\rho$  values, approximately  
199 from 1 to 6; the histograms have maximums near  $\rho \approx 2$  and sharply decline with decreasing  
200 and increasing  $\rho$ . Figs. 2 and 3 show daytime and nighttime global biases and SDs of the  
201 BSST and PWR SST, as functions of  $\rho$ . The statistics are relatively stable in the range  $1 < \rho <$   
202  $6$ , and less so outside this interval, due to decreasing density of matchups (cf. Fig. 1). Note  
203 that  $\rho$  is not necessarily equal to  $V(\delta T_S)^{0.5}$ , as predicted by Eq. (7) for an ideal case of standard  
204 Gaussian error of the regression SST. However, the SDs in Figs. 2-3 near-monotonically  
205 increase with  $\rho$  within the interval of stability, for all sensors and for both BSST and PWR  
206 SST, during both day and night, adding confidence in the selection of  $\rho$  as the characteristic  
207 variable of the SSES parameterization. Note also that compared with the BSSTs, the PWR  
208 SSTs consistently produce more uniform biases and smaller SDs, which are additionally more  
209 consistent between different sensors.

The segmentation of the SST domain is performed by partitioning each orthant of the  $\mathbf{R}$ -space into 10 bins with values of Fisher distance falling into the intervals  $j-1 < \rho \leq j, j=1,2,\dots, 10$ . Given  $N$  is the dimensionality of  $\mathbf{R}$ , the total number of segments is  $10 \times 2^N$ , which corresponds to 640 segments for the daytime and 5,120 segments for the nighttime algorithms. The number of matchups in these subsets is quite non-uniform, ranging from 0 to several thousands. SSES SDs and local regression coefficients are only calculated for “populated” segments which include more than 10 matchups. Table 2 also shows the total numbers of populated segments and the percentages of matchups belonging to the “unpopulated” segments with 10 matchups or less. The number of populated segments in all cases is much less than the total numbers of considered segments. The fraction of matchups falling into the unpopulated segments is 0.2-0.3 % for day and reaches 2-3% for night, due to more detailed segmentation of the nighttime  $\mathbf{R}$ -space. For the unpopulated segments SSES biases are set to 0 and SSES SDs are filled with not-a-number (NaN) values indicating that the corresponding SSES estimates are unavailable.

When processing satellite data, the local regression coefficients are used to calculate the PWR SST. Special measures are taken to avoid amplification of PWR SST errors caused by calculation of coefficients from a small subset of matchups. Vectors  $\mathbf{f}$  of local regression coefficients are calculated as follows:

$$\mathbf{f} = \mathbf{E}^{-1} \langle \langle (\mathbf{X} - \langle \mathbf{X} \rangle) (T_{in\ situ} - \langle T_{in\ situ} \rangle) \rangle \rangle \quad (13)$$

Here,  $\langle \langle * \rangle \rangle$  denotes averaging over a given subset of matchups;  $\mathbf{E}$  is a matrix constructed from the local covariance matrix of regressors  $\mathbf{F}$  by omitting the eigenvectors corresponding to the eigenvalues smaller than  $k\lambda_{max}$  (where  $\lambda_{max}$  is the maximum eigenvalue of  $\mathbf{F}$ ). The value

of the multiplier  $k=10^{-8}$  has been chosen empirically to provide a reasonable tradeoff between the accuracy of fitting *in situ* SST with PWR SST and the amplification of random noise in PWR SST. As a result, the number of degrees of freedom for the estimated vector of coefficients is usually less than the number of regressors,  $N$ .

The local regression coefficients and SSES SDs for all segments are stored in the LUT along with other data required for calculation of  $\rho$  and attributing pixels to the specific orthants in the  $\mathbf{R}$ -space:  $\langle \mathbf{R} \rangle$ , eigenvalues and eigenvectors of  $\mathbf{D}$ . In ACSPO operational processing, each pixel is first ascribed to a specific segment. If the SSES SD for this segment is not NaN, then the following procedures are performed for this pixel: 1) PWR SST is calculated using the local regression coefficients; 2) SSES bias is calculated as BSST minus PWR SST; 3) SSES SD is set to the corresponding LUT value. Otherwise, if the LUT value of SSES SD is NaN, then SSES bias is set to 0 and SSES SD is set to NaN for this pixel. We expect that this algorithm will be further optimized in the future versions of ACSPO.

#### **4. The performance of SSES bias correction**

As stated in Section 3, the SSES bias is defined as difference between the BSST and the PWR SST. Applying the SSES biases to the BSST transforms it back into the PWR SST. Hence, the PWR SST is an equivalent of the de-biased BSST. In this section, we evaluate the performance of the SSES bias correction by comparing the statistics of BSST and PWR SST with respect to *in situ* SST and illustrate it with results of processing satellite data with the ACSPO v. 2.40.

Table 3 compares global statistics of fitting *in situ* SST with the BSST and PWR SSTs over the full global MDS collected for six satellite sensors from 15 May 2013 to 8 August 2014, as

described in Section 3. Table 3 also shows the equator crossing times (ECT) for these sensors. Since, in this case, the same MDS were used for both training and validation the global biases for both algorithms are 0. The PWR SST fits *in situ* SST substantially more precisely than the BSST: the corresponding SDs are reduced from 0.41 K – 0.50 K to 0.31 K – 0.34 K for the daytime, and from 0.33-0.46 K to 0.25 – 0.30 K for the nighttime. Table 3 also shows the statistics of fitting the same *in situ* SSTs with the CMC SST, interpolated to satellite pixels. Recall that the CMC is a foundation SST produced from the nighttime data. Therefore, it is well consistent with the nighttime satellite data (although slightly biased cold with respect to the nighttime matchups for the morning platforms Terra, Metop-A and Metop-B), but significantly biased cold with respect to daytime matchups for the afternoon platforms S-NPP, Aqua and NOAA-19. The PWR SSTs makes the global SDs with respect to matchups comparable to (or even smaller than) the corresponding SDs for CMC but does not produce global biases typical for CMC.

In addition to the metrics commonly used to evaluate the performance of the SST algorithms, bias and SD with respect to *in situ* SST, Merchant et al. (2009) introduced another informative metric – sensitivity of retrieved SST to variations in true SST. This analytical metric is calculated by replacing observed BTs in the regression equation with simulated derivatives of the BTs in terms of SST, and setting the corresponding offset to 0. This metric, however, is not fully applicable to the PWR SST. The input for existing radiative transfer models, such as the Community Radiative Transfer Model (CRTM – available online at <http://ftp.emc.ncep.noaa.gov/jcsda/CRTM/>) is “skin” SST, i.e, the temperature of the upper ~10  $\mu$ m layer of the ocean rather than “depth” SST measured by drifting and moored buoys (Donlon et al. 2007). Therefore, the theoretically estimated sensitivity characterizes the

response of satellite SST retrievals to “skin” rather than “depth” SST. On the other hand, the fact that the PWR SST precisely fits *in situ* SST suggests that it may be rather viewed as an estimate of “depth” SST. In this study, we evaluate the responses of BSST and PWR SST to variations in “depth” (rather than “skin”) SST, using a squared correlation coefficient  $\eta^2$  between the satellite and *in situ* SSTs. The meaning of  $\eta^2$  may be explained with the following relationship between the full variance of  $T_s$ ,  $V_o(T_s)$ , and the residual variance of the regression between satellite and *in situ* SST,  $V(T_s)$  (Bard, 1974):

$$V(T_s) = V_o(T_s)(1 - \eta^2). \quad (14)$$

As follows from Eq. (14),  $\eta^2$  characterizes a part of the  $V_o(T_s)$  explained by variations in *in situ* SST.

Figs. 4 and 5 show geographical distributions of the biases, SDs and squared correlations for VIIRS BSST and PWR SST produced from the global MDS by aggregating matchups within  $10^\circ \times 10^\circ$  lat/lon boxes. Daytime BSST biases in Fig. 4 are mostly within 0 - 0.1 K in the mid-latitudes but significantly positive in the Southern high latitudes and negative in the Tropics (between 0 and  $20^\circ$  N) and to the North of  $60^\circ$  N. The PWR SST reduces the negative biases in the low latitudes, and to a lesser degree the positive biases in the Southern high latitudes. The biases in the North and in the South, however, remain significant. This will be a subject of future work. The reduction in daytime SDs from BSST to PWR SSTs is 0.1 – 0.2 K over the most part of the global ocean. The squared correlation between the BSST and *in situ* SST has a minimum in the Tropics, likely due to the effects of daytime surface warming and large atmospheric humidity, which significantly reduces the effect of SST at the top of atmosphere. The PWR SST is better than BSST correlated with buoys in the low latitudes. The nighttime



regional statistics shown in Fig. 5 demonstrate similar features, but with lesser difference between BSST and PWR SST, because the nighttime SST algorithm uses a much more transparent band centered at 3.7  $\mu\text{m}$  and due to the absence of the effect of the daytime surface warming.

The described SSES methodology was implemented in ACSPO version 2.40 and used in L2 processing of satellite data. According to the methodology described in Section 3, the SSES are defined during training for those pixels which belong to the “populated” segments represented in the training MDS with more than 10 matchups. This has allowed providing the SSES estimates for the overwhelming part of the clear-sky ocean pixels. As an example, the relative fractions of the clear-sky SST pixels with undefined SSES are shown in Table 4 from one day (31 January 2015) of observations with six sensors. The numbers in Table 4 are well consistent with the fractions of matchups falling in the “unpopulated” segments shown in Table 2.

Fig.6 and 7 show results of validation of BSST and PWR SST using the independent datasets of matchups. Fig. 6 shows time series of daytime biases and SDs for the BSST, PWR SST and CMC SST with respect to *in situ* SST for six sensors from 24 November 2014 to 10 March 2015. All curves were smoothed with a 7-day running window. To discern the difference in the effects of the diurnal surface warming on the sensors with different ECT, only those matchups were used for which the time difference between satellite and *in situ* SST measurements did not exceed 1 hour. The daytime statistics for PWR SST in Fig. 6 are more stable and consistent between the sensors than the statistics for BSST. The peak-to-peak ranges for the global SDs are reduced from ~0.35 K-0.52 K for BSST to ~0.27 K-0.38 K for PWR SST. The corresponding biases in the foundation CMC SST are close to zero for the

mid-morning MetOp-A and -B satellites, slightly negative for the late-morning Terra, and close to - 0.2 K for the afternoon S-NPP, Aqua and NOAA-19. The PWR SST brings global daytime SDs close to the CMC but, unlike CMC, it produces small and more consistent biases for all platforms. This suggests that daytime ACSPO SSTs corrected for SSES bias can be now assimilated in the L4 analyses, on equal footing with the nighttime data (recall that current L4s exclude daytime data with low winds from analyses) and even used to produce a daytime foundation L4 SST product, with performance comparable with the existing L4 SSTs produced from nighttime SST retrievals.

Fig. 7 shows similar time series for night. As in Fig. 6, the PWR SST reduces global biases and SDs compared with the BSST, and improves cross-platform consistency of the statistics. The nighttime CMC biases are more consistent between the sensors than during daytime, although the biases for the mid-morning platforms MetOp-A, -B and Terra are now colder than for the afternoon platforms S-NPP, Aqua, NOAA-19. As for the daytime, the nighttime global SDs of PWR SST CMC SST, are both much lower than for the BSST.

It is important to note that the correction of SSES biases in the ACSPO v. 2.40 provides the reduction of instantaneous biases in every given SST image. Fig.8 demonstrates the effect of the daytime bias correction by comparing the images of BSST minus CMC, SSES bias and PWR SST minus CMC in a swath projection taken over the Equatorial Pacific Ocean on 19 December 2014. Cloud leakages in BSST are seen in the left image as a fringe of colder pixels surrounding clouds, whereas areas with warm deviations of BSST from CMC SST are due to diurnal surface warming. The image in the middle demonstrates that the SSES bias effectively captures both effects. As a result, the biases are reduced in the right image showing the deviations of PWR SST from CMC.

Fig. 9 shows an example of nighttime imagery in the swath projection. The left image shows typical angular artifacts in BSST minus CMC. The BSST is slightly colder than CMC SSTs in the middle and at the edges of the swath, and slightly warmer at intermediate VZAs. Cold biases caused by cloud leakages are also present. The SSES bias shown in the middle effectively accounts for both artifacts in the BSST, which makes the deviations of the PWR SST from CMC more flat and uniform.

Fig. 10 demonstrates the effects of SSES bias correction on the deviations of ACSPO SST from CMC SST for S-NPP VIIRS observations on 16 February 2015. The deviations of BSST from CMC are mainly caused by cloud leakages and by variations in VZA. During the daytime, warming in the upper surface layer of the ocean is another factor. SSES biases capture all these effects, to a different degree. The SSES bias correction appears efficient, as evidenced by noticeably more uniform images of the PWR SST – CMC SST compared with the BSST – CMC SST. Note that Fig. 10 represents a stringent test in the full VIIRS retrieval domain for the SSES which was developed from match-ups with *in situ* data which are only available in its constrained sub-space.

## **5. Summary and conclusions**

The redesigned ACSPO SSES algorithm defines bias of the baseline SST product (BSST, estimated with Eq. 1 and 2) as difference between the BSST and the piecewise regression SST, PWR SST, introduced in this study. Applying SSES biases to the BSST transforms it back into the PWR SST. Comparison of the performance of the BSST and PWR SST shows that the SSES bias correction substantially improves a global agreement with *in situ* SST. This is achieved by 1) segmentation of the SST retrieval domain in the space of regressors (rather

than in the space of physical variables as is the customary practice in the SST community), 2) deriving the segmentation criteria from the statistical structure of regressors within the training MDS; and 3) defining the de-biased BSST as PWR SST calculated with local regression coefficients, separately derived for each segment.

The performance of the ACSPO PWR SST gives a new perspective to the question, to which extent the precision of fitting *in situ* SST with global regression SST algorithm can be improved by stratification of regression coefficients. The piecewise regression methodology was previously implemented in Pathfinder AVHRR and NASA MODIS SST processing (Evans and Podesta 1998; Kilpatrick et al. 2001, 2015; Casey et al. 2010) and in the more recent LATBAND (Minnett and Evans 2009) algorithms. In the current Pathfinder AVHRR SST product, regression coefficients are stratified in terms of BT difference between 11  $\mu\text{m}$  and 12  $\mu\text{m}$  bands, considered a proxy for the atmospheric humidity. LATBAND introduces separate sets of coefficients for each of 20° latitudinal bands. Both these algorithms have reduced global SD with respect to *in situ* SST by ~ 0.02 K compared to the case of using the same equation with a single global set of coefficients (Table 2 in [Petrenko et al. 2014b](#)). In the redesigned ACSPO SSES algorithm, the PWR SST reduces global SD by 0.10-0.15 K during the day and by 0.08-0.15 K at night, bringing the global SDs in the satellite retrieved PWR SST to the level typical for “foundation” L4 SST products, such as the CMC or Operational Sea Surface Temperature and Sea Ice Analysis (OSTIA - Donlon et al. 2012).

Thus, the ACSPO version 2.40 effectively provides users with two SST products, the BSST and the PWR SST. The PWR SST is not reported in the output ACSPO files as a separate layer, but can be easily obtained by subtracting the SSES bias from the BSST. These two products have different characteristics. The BSST provides a reasonable combination of

precision with respect to *in situ* SST and sensitivity to “skin” SST ([Petrenko et al. 2014b](#)). The PWR SST correlates and agrees with *in situ* SST much better than does the BSST, but it does not guarantee high sensitivity to “skin” SST. Therefore, the PWR SST can be viewed as an estimate of “depth” SST.

A full range of potential applications of the PWR SST is yet to be determined. In particular, it is expected to benefit producers of the “foundation” (CMC, OSTIA) and “depth” (Reynolds) L4 SSTs, by reducing or eliminating the need in the L4-specific “bias correction” during assimilation of ACSPO SST data. The fact that the global precision of daytime PWR SST is now comparable with the precision of L4 SST (with the additional bonus of not showing sensor-dependent biases with respect to matchups) suggests that daytime ACSPO SST can be now successfully assimilated in the L4 SST, similarly to the nighttime retrievals, or can be used to create a daytime L4 SST from the daytime PWR SST. We emphasize, however, that although all analyses in this study consistently suggest that the new ACSPO SSES should be of interest to L4 producers and have a positive effect on their analyses, the ultimate test is assimilation in L4. Work is currently underway with different L4 groups, and its results will be reported elsewhere.

Along with SSES bias, which was discussed in this study in details, the ACSPO v. 240 also reports SSES SD estimated as SD of BSST minus *in situ* SST for specific segments. The performance of the SSES SD is yet to be evaluated. This can be done, for example, by using it to better define the optimal weights with which BSST should be assimilated into the L4 SST product. Note that the SSES SD for the PWR SST has not been included in the ACSPO v.2.40 output because the GDS 2.0 format only allows for one SSES set. However, SSES SD for the PWR SST may be easily added to the ACSPO output per users’ request. The redesigned SSES

algorithm presented in this paper and implemented in the version 2.40 of ACSPO should not be considered a final version and will be further optimized in the future. At this point of time, the following potential areas of improvement are envisioned.

1. The fundamental limitation of the segmentation algorithm is that some of the segments are represented within the training MDS with insufficient numbers of matchups. This makes the SSES estimates for such segments less reliable. The current SSES LUTs have been derived from MDS covering more than a year-long time period from 15 May 2013 – 8 August 2014. This time period may be further extended to ensure better coverage of the problematic segments, provided that the sensor’s calibration remains stable.
2. More detailed segmentation of the SST domain might allow for better discrimination of the SSES for different observational conditions, but it would further reduce reliability of SSES estimates due to reducing the number of matchups belonging to each segment. Further optimization of the segmentation algorithm will be explored for a better tradeoff between the two factors mentioned above.
3. Visual analysis of the PWR SST imagery shows that most of the images do not include discernible artifacts and discontinuities, although they are often composed from different segments with different local regression coefficients and SSTs. However, the possibility of such undesirable effects is not excluded. This problem also will be addressed in the next version of ACSPO.
4. In addition to SSES, the GDS2 format requires assessing the quality of L2 SST pixels using an incremental scale from 0 to 5, where 0 corresponds to the worst quality and 5 indicates the best quality data. Currently, the definitions of quality levels in

ACSPO are independent from SSES and based on the ACSPO clear-sky mask (Petrenko et al., 2010): levels 5 and 4 correspond to respectively “clear” and “probably clear” pixels, and level 0 is assigned to all other pixels. In Section 2 we introduced additional metric for the quality of the SST estimate - Fisher distance, which directly links the standard deviation of a given SST estimate to the structure of the training MDS. In the future this parameter can be used for further specification of the ACSPO quality levels.

## 6. Acknowledgments

This work was conducted under the JPSS and Geostationary Operational Environmental Satellite-R Series (GOES-R) SST Projects funded by the JPSS and GOES-R Program Offices, respectively. We thank JPSS Program Scientist Mitch Goldberg and GOES-R Manager, Jaime Daniels. We also appreciate support of the NOAA Ocean Remote Sensing Program (Program Manager: Paul DiGiacomo). Thanks also go to our NOAA colleagues John Sapper, John Stroup, Xingming Liang, Xinjia Zhou and Feng Xu for assistance, discussions, and feedback at its different stages. The views, opinions, and findings contained in this paper are those of the authors and should not be construed as an official NOAA or US Government position, policy, or decision.

## 7. References

Bard, Y., 1974: *Nonlinear parameter estimation*. Academic Press, New York, 351 pp.

- 456 [Brasnett, B., 2008: The impact of satellite retrievals in a global sea-surface-temperature](#)  
 457 [analysis. \*Q. J. R. Meteorol. Soc.\*, \*\*134\*\*, 1745-1760, doi: 10.1002/qj.319.](#)
- 458 [Bury, K.V., 1975: \*Statistical models in applied science\*. John Wiley & Sons, New York –](#)  
 459 [London – Sydney – Toronto, 625 p.](#)
- 460 Casey, K.S., T.B. Brandon, P. Cornillon, and R. Evans, 2010: The past, present and future of  
 461 the AVHRR Pathfinder program. *Oceanography from Space*, Springer, doi:10.1007/978-  
 462 90-481-5\_16, 323-341. [Available online at  
 463 [http://www.nodc.noaa.gov/SatelliteData/pathfinder4km/OFS\\_21\\_Cas\\_09Dec2009.pdf](http://www.nodc.noaa.gov/SatelliteData/pathfinder4km/OFS_21_Cas_09Dec2009.pdf).]
- 464 Castro, S., G. Wick, D. Jackson, and W. Emery, 2008: Error characterization of infrared and  
 465 microwave sea surface temperature products for merging and analysis. *J. Geophys. Res.*,  
 466 **113**, C03010, doi:10.1029/2006JC003829.
- 467 [Cayula, J.F., D. May, B. McKenzie, D. Olszewski, and K. Willis, 2004: Reliability estimates](#)  
 468 [for real-time sea surface temperature. \*Sea Technology Magazine\*, Feb 2004, 67-73.](#)
- 469 Donlon, C., N. Rayner, I. Robinson, et al., 2007: The Global Ocean Data Assimilation  
 470 Experiment High-resolution Sea Surface Temperature Pilot Project. *Bull. Amer. Meteor.*  
 471 *Soc.*, **88**, 1197–1213, doi: 10.1016/j.rse.2010.10.017.
- 472 [Donlon, C., M. Martin, J. Stark, J. Roberts-Jones, E. Fiedler, and W. Wimmer, 2012: The](#)  
 473 [operational sea surface temperature and Sea Ice Analysis \(OSTIA\) system. \*Remote Sens.\*](#)  
 474 [Environ.](#), **116**, 140–158, doi: 10.1016/j.rse.2010.10.017.



475 Evans, R., and G. Podesta, 1998: Pathfinder sea surface temperature algorithm. U. Miami,  
 476 Rosenstiel School of Marine and Atmospheric Science. [Available online at  
 477 [http://yyy.rsmas.miami.edu/groups/rsl/pathfinder/Algorithm/algo\\_index.html](http://yyy.rsmas.miami.edu/groups/rsl/pathfinder/Algorithm/algo_index.html)]

478 Griffin, C., 2014: ABoM AVHRR SSES. Proceedings of the GHR SST XV Science Team  
 479 Meeting, Cape Town, South Africa, 2-6 June 2014, p.197. [Available online at  
 480 [https://www.ghrsst.org/documents/q/category/ghrsst-science-team-meetings/ghrsst-xv-](https://www.ghrsst.org/documents/q/category/ghrsst-science-team-meetings/ghrsst-xv-cape-town-south-africa/)  
 481 [cape-town-south-africa/](https://www.ghrsst.org/documents/q/category/ghrsst-science-team-meetings/ghrsst-xv-cape-town-south-africa/)]

482 Kilpatrick, K.A., G.P. Podesta, and R. Evans, 2001: Overview of the NOAA/NASA advanced  
 483 very high resolution radiometer Pathfinder algorithm for sea surface temperature and  
 484 associated matchup database, *J. Geophys. Res.*, **106**, C5, 9179-9297.

485 [Kilpatrick, K.A., G. Podestá, S. Walsh, E. Williams, V. Halliwell, M. Szczodrak, O.B. Brown,](#)  
 486 [P.J. Minnett and R. Evans, 2015: A decade of sea surface temperature from MODIS,](#)  
 487 [Remote Sens Environ.](#), **165**, (8), 27-41, doi: 10.1016/j.rse.2015.04.023

488 Kozlov, V.P., 1966: On the estimation of the vertical temperature profile from the outgoing  
 489 radiation spectrum, *Izv. Acad. Sci. USSR Atmos. Oceanic Phys.*, **2**, 80.

490 Lavanant, L., P. Le Borgne, and G. Legendre, 2012: VIIRS SST at OSI-SAF, GHR SST XIII  
 491 Science Team Meeting, Tokyo, Japan, p. 235. [Available online at  
 492 [https://www.ghrsst.org/documents/q/category/ghrsst-science-team-meetings/ghrsst-xiii-](https://www.ghrsst.org/documents/q/category/ghrsst-science-team-meetings/ghrsst-xiii-tokyo-japan/proceedings/)  
 493 [tokyo-japan/proceedings/](https://www.ghrsst.org/documents/q/category/ghrsst-science-team-meetings/ghrsst-xiii-tokyo-japan/proceedings/)]

494 [Merchant C J, P Le Borgne, A Marsouin and H Roquet, 2008: Optimal estimation of sea](#)  
 495 [surface temperature from split-window observations, \*Remote. Sens. Environ.\*, \*\*112\*\* \(5\),](#)  
 496 [2469-2484, doi:10.1016/j.rse.2007.11.011.](#)

497 [Merchant, C.J., A.R. Harris, H. Roquet, and P. Le Borgne, 2009: Retrieval characteristics of](#)  
 498 [non-linear sea surface temperature from the Advanced Very High Resolution](#)  
 499 [Radiometer, \*Geophys. Res. Lett.\*, \*\*36\*\*, L17604, doi: 10.1029/2009GL039843.](#)

500 Minnett, P.J., and R.H. Evans, 2009: MODIS sea-surface temperatures, GHR SST Users'  
 501 Symposium, Santa Rosa, CA, USA, 28-29 May 2009. [Available online at  
 502 [https://www.ghrsst.org/files/download.php?m=documents&f=Session2\\_Minnett.ppt](https://www.ghrsst.org/files/download.php?m=documents&f=Session2_Minnett.ppt).

503 Minnett, P.J., 2014: MODIS/VIIRS hypercube, Proceedings of the GHR SST XV Science  
 504 Team Meeting, Cape Town, South Africa, 2-6 June 2014, p.197. [Available online at  
 505 [https://www.ghrsst.org/documents/q/category/ghrsst-science-team-meetings/ghrsst-xv-](https://www.ghrsst.org/documents/q/category/ghrsst-science-team-meetings/ghrsst-xv-cape-town-south-africa/)  
 506 [cape-town-south-africa/](https://www.ghrsst.org/documents/q/category/ghrsst-science-team-meetings/ghrsst-xv-cape-town-south-africa/)]

507 OSI-SAF Low Earth Orbiter Sea Surface Temperature Product User Manual, Version 2.1, The  
 508 EUMETSAT Network of Satellite Application Facilities, OSI-SAF, 2009: [Available  
 509 online at [http://www.osi-saf.org/biblio/docs/ss1\\_pum\\_leo\\_sst\\_2\\_1.pdf](http://www.osi-saf.org/biblio/docs/ss1_pum_leo_sst_2_1.pdf)]

510 Petrenko, B., A. Ignatov, Y. Kihai, and A. Heidinger, 2010: Clear-sky mask for the Advanced  
 511 Clear-Sky Processor for Oceans, *J. Atm. Oceanic Tech.*, **27**, 1609–1623, doi:  
 512 10.1175/2010JTECHA1413.1.

513 Petrenko, B. and A. Ignatov, 2014a: SSES in ACSPO, Proceedings of the GHR SST XV  
 514 Science Team Meeting, Cape Town, South Africa, 2-6 June 2014, pp.219-220,

515 [Available online at [https://www.ghrsst.org/documents/q/category/ghrsst-science-team-](https://www.ghrsst.org/documents/q/category/ghrsst-science-team-meetings/ghrsst-xv-cape-town-south-africa/)

516 [meetings/ghrsst-xv-cape-town-south-africa/](https://www.ghrsst.org/documents/q/category/ghrsst-science-team-meetings/ghrsst-xv-cape-town-south-africa/)]

517 Petrenko, B., A. Ignatov, Y. Kihai, J. Stroup, and P. Dash, 2014b: Evaluation and selection of

518 SST regression algorithms for JPSS VIIRS, *J. Geophys. Res.*, **119**, 4580–4599,

519 doi:[10.1002/2013JD020637](https://doi.org/10.1002/2013JD020637).

520 Proceedings of the GHRSSST XV Science Team Meeting, Cape Town, South Africa, 2-6 June

521 2014, pp. 197-199. [Available online at

522 [https://www.ghrsst.org/documents/q/category/ghrsst-science-team-meetings/ghrsst-xv-](https://www.ghrsst.org/documents/q/category/ghrsst-science-team-meetings/ghrsst-xv-cape-town-south-africa/)

523 [cape-town-south-africa/](https://www.ghrsst.org/documents/q/category/ghrsst-science-team-meetings/ghrsst-xv-cape-town-south-africa/)]

524 Reynolds, R.W., N.A. Rayner, T.M. Smith, D.C. Stokes, and W. Wang, 2002: An improved in

525 situ and satellite SST analysis for climate. *J. Climate*, **15**, 1609–1625, doi:

526 [http://dx.doi.org/10.1175/1520-0442\(2002\)015%3C1609:AIISAS%3E2.0.CO;2](http://dx.doi.org/10.1175/1520-0442(2002)015%3C1609:AIISAS%3E2.0.CO;2)

527 Xu, F., and A. Ignatov, 2014 : In situ SST Quality Monitor (iQuam), *J. Atmos. Oceanic Tech.*,

528 **31**, 164-180, doi:10.1175/JTECH-D-13-00121.1.

529 Xu, F., A. Ignatov, and X. Liang, 2009 : Towards continuous error characterization of SST in

530 ACSPO, 89<sup>th</sup> AMS Annual Meeting, Phoenix, AZ, 12-16 January 2009. [Available online

531 at: [ams.confex.com/ams/89annual/webprogram/Paper143882.html](http://ams.confex.com/ams/89annual/webprogram/Paper143882.html)]



533

## **Tables**

534

535 Table 1. Acronyms used in this paper.

ACSP0	Advanced Clear-Sky Processor for Oceans
AVHRR	Advanced Very High Resolution Radiometer
BT	Brightness temperature
CMC	Canadian Met Center
GAC	Global Area Coverage mode
CRTM	Community Radiative Transfer Model
GHRSSST	Group for High Resolution SST
ECT	Equator crossing time
EUMETSAT	European Organization for the Exploitation of Meteorological Satellites
FRAC	Full Resolution Area Coverage mode
GDS2	GHRSSST Data Specification Revision 2.0
iQuam	<i>In situ</i> Quality Monitor
L2	Level 2
L4	Level 4
LUT	Look-up table
MDS	Data set of matchups
MODIS	Moderate Resolution Imaging Spectroradiometer
NASA	National Aeronautics and Space Administration
NAVO	Naval Oceanographic Office
NOAA	National Oceanic and Atmospheric Administration
OSI SAF	Ocean and Sea Ice Satellite Application Facility
OSTIA	Operational Sea Surface Temperature and Sea Ice Analysis
PDF	Probability density function
PWR SST	Piecewise Regression SST

---

S-NPP VIIRS	Suomi National Polar-orbiting Partnership
<b>R</b> -space	Space of regressors
TPW	Total precipitable water vapor content in the atmosphere
SD	Standard deviation
SSES	Sensor-Specific Error Statistics
SR SST	Standard Regression SST
SST	Sea surface temperature
VIIRS	Visible Infrared Imaging Radiometer Suite
VZA	Satellite view zenith angle

---

536

537 Table 2. Total numbers of matchups in the global MDS collected from 15 May 2013 – 8  
 538 August 2014, total numbers of “populated” segments including more than 10 matchups and  
 539 the percentages of matchups belonging to the “unpopulated” segments including 10 or less  
 540 matchups.

Day/Night	S-NPP	Aqua	Terra	MetOp-A	MetOp-B	NOAA19
	VIIRS	MODIS	MODIS	AVHRR	AVHRR	AVHRR
. Total number of matchups in the MDS						
Day	108,355	85,534	85,065	104,047	107,440	92,823
Night	113,796	85,574	89,757	120,068	116,549	94,284
Total number of segments with more than 10 matchups						
Day	202	201	199	202	206	204
Night	789	764	760	796	850	830
Percentage of matchups belonging to the segments with no more than 10 matchups						
Day	0.22%	0.28%	0.24%	0.25%	0.23%	0.32%
Night	2.65%	3.52%	3.12%	2.56%	2.67%	3.37%

541



Table 3. The equator crossing times (ECT), global biases and SDs of fitting in situ SST with BSST, PWR SST and CMC SST over the full MDS collected from 15 May 2013 – 8 August 2014, for six sensors.

SST Product	Statistics (Kelvin)	S-NPP VIIRS	Aqua MODIS	NOAA19 AVHRR	Terra MODIS	MetOp-A AVHRR	MetOp-B AVHRR
ECT		1:30 pm	1:30 pm	1:30 pm	10:30 am	9:30 am	9:30 am
Day							
BSST	Bias	0	0	0	0	0	0
	SD	0.41	0.45	0.50	0.46	0.43	0.44
PWR SST	Bias	0	0	0	0	0	0
	SD	0.31	0.33	0.34	0.32	0.31	0.30
CMC SST	Bias	-0.19	-0.20	-0.21	-0.06	-0.01	-0.01
	SD	0.34	0.34	0.35	0.31	0.30	0.30
Night							
BSST	Bias	0	0	0	0	0	0
	SD	0.33	0.35	0.46	0.35	0.38	0.36
PWR SST	Bias	0	0	0	0	0	0
	SD	0.25	0.26	0.29	0.26	0.27	0.26
CMC SST	Bias	0.01	0.02	0.02	-0.04	-0.07	-0.07
	SD	0.27	0.28	0.29	0.29	0.31	0.29

547 Table 4. The fractions of clear-sky pixels in which SSES SD is not defined, for six sensors (31  
 548 January 2015)

Day/Night	S-NPP	Aqua	Terra	MetOp-A	MetOp-B	NOAA19
	VIIRS	MODIS	MODIS	AVHRR	AVHRR	AVHRR
Day	0.52%	0.37%	0.22%	0.41%	0.32%	0.63%
Night	2.07%	2.34%	2.14%	2.25%	2.52%	2.66%

549

550

551

## Figure Caption List

Fig.1. Histograms of Fisher distance produced from daytime and nighttime matchups within the global MDS collected from 15 May 2013 – 8 August 2014 (bin size  $\Delta\rho = 1.0$ ).

Fig. 2. Daytime (a, b) biases and (c, d) SDs of (a, c) BSST and (b, d) PWR SSTs wrt. *in situ* SST as functions of Fisher distance. Data from the same MDS as in Fig.1.

Fig.3. Same as in Fig. 2 but for nighttime data.

Fig. 4. Daytime statistics of: (left) BSST and (right) PWR SSTs wrt. *in situ* SST, stratified within  $10^\circ \times 10^\circ$  lat/lon boxes. (Top) biases; (middle) SDs; (bottom) squared correlation coefficients.

Fig.5. Same as in Fig. 4 but for nighttime.

Fig. 6. Time series of daily daytime global biases and SDs of fitting *in situ* SST with BSST, PWR SST and CMC, for six satellite sensors, from 24 November 2014 to 10 March 2015.

Fig.7. Same as in Fig. 4 but for nighttime.

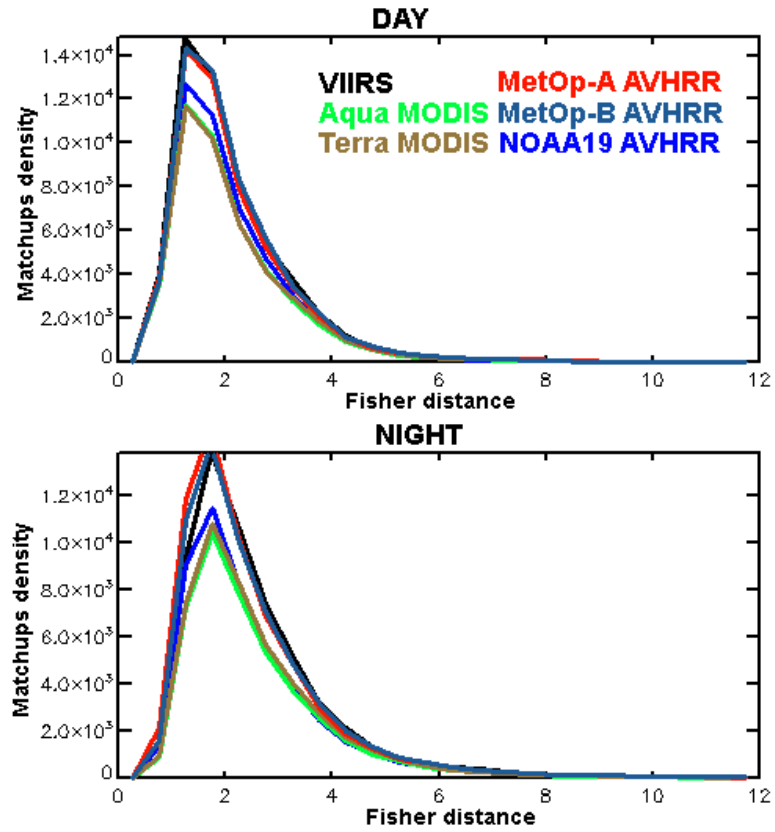
Fig.8. Daytime images of BSST – CMC SST, PWR SST – CMC SST and SSES bias in swath projection from S-NPP VIIRS on 19 December 2014 over the Equatorial Pacific Ocean.

Fig. 9. Nighttime images of BSST – CMC SST, SSES bias and PWR SST – CMC SST in swath projection produced from S-NPP VIIRS observations on 19 December 2014 over the Equatorial Pacific Ocean.

570 Fig.10. (Left panels) daytime and (right panels) nighttime geographical distributions of (top)  
571 BSST-CMC SST, (middle) SSES bias, (bottom) PWR SST- CMC SST from S-NPP VIIRS  
572 observations on 16 February 2015.

573

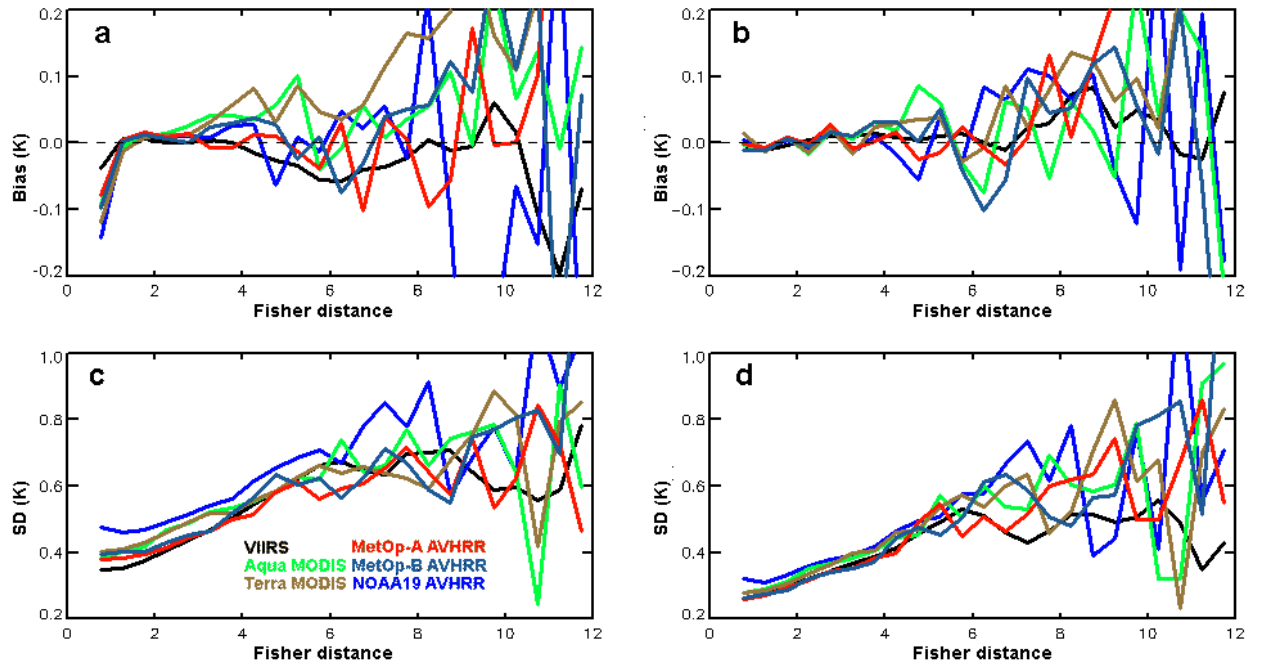




575

576 Fig.1. Histograms of Fisher distance produced from daytime and nighttime matchups within  
 577 the global MDS collected from 15 May 2013 – 8 August 2014 (bin size  $\Delta\rho = 1.0$ ).

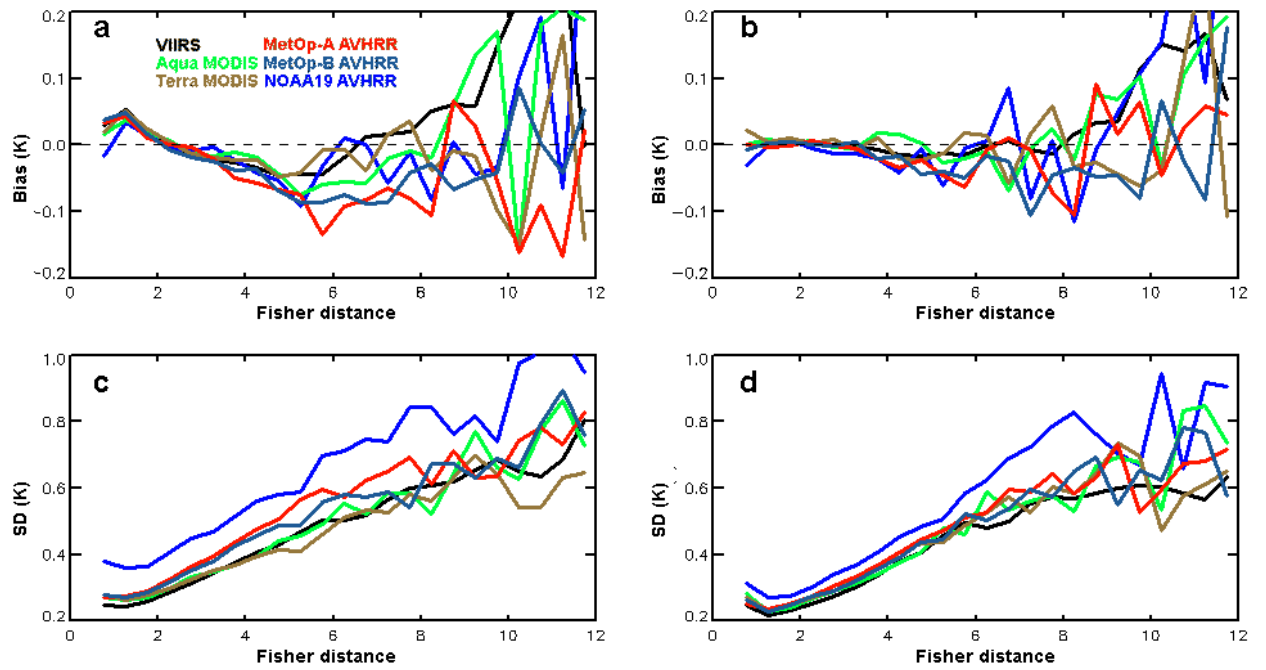
578



579

580 Fig. 2. Daytime (a, b) biases and (c, d) SDs of (a, c) BSST and (b, d) PWR SSTs wrt. *in situ*

581 SST as functions of Fisher distance. Data from the same MDS as in Fig.1.



582

583 Fig.3. Same as in Fig. 2 but for nighttime data.



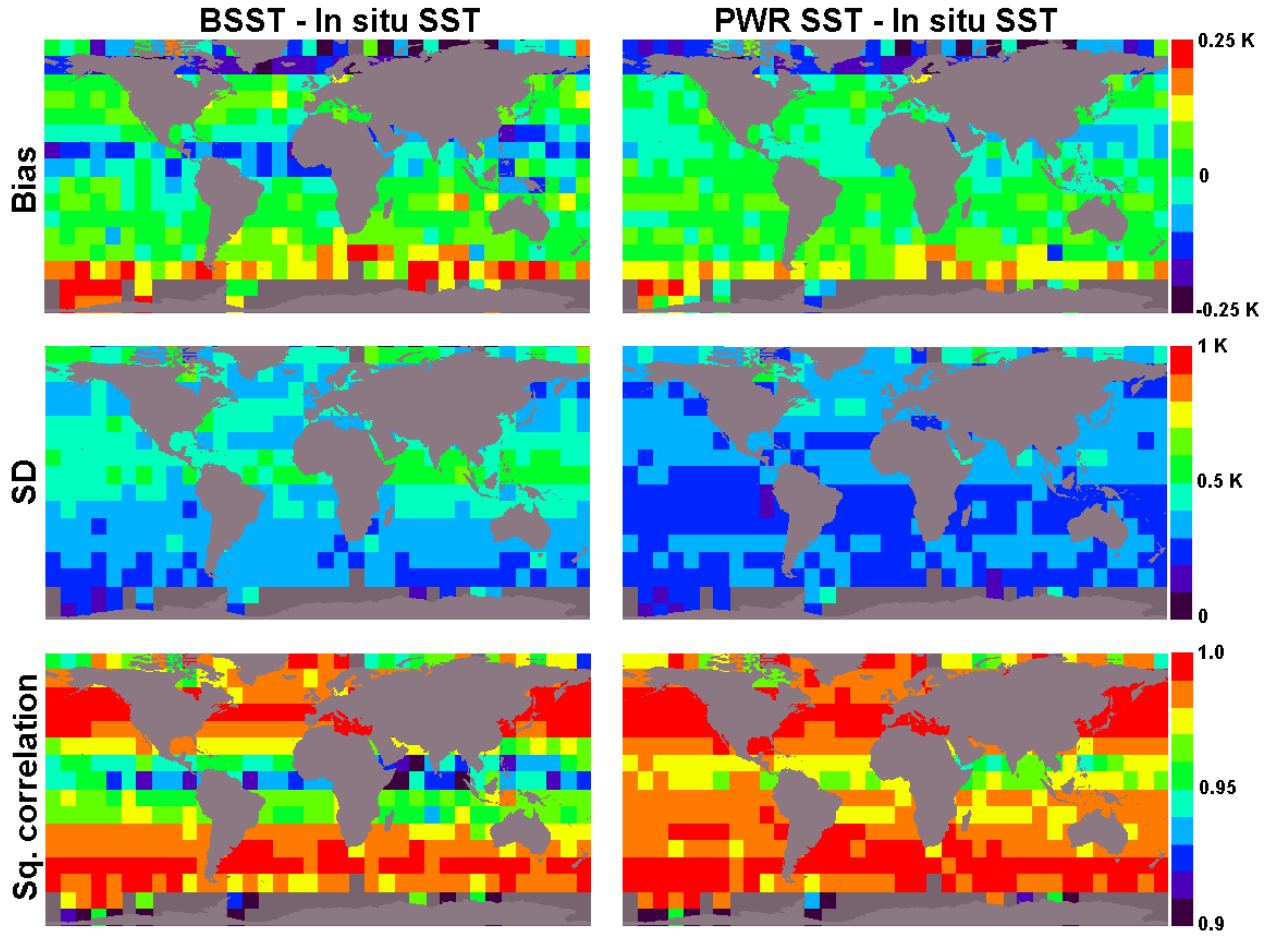


Fig. 4. Daytime statistics of: (left) BSST and (right) PWR SSTs wrt. *in situ* SST, stratified within  $10^{\circ} \times 10^{\circ}$  lat/lon boxes. (Top) biases; (middle) SDs; (bottom) squared correlation coefficients.

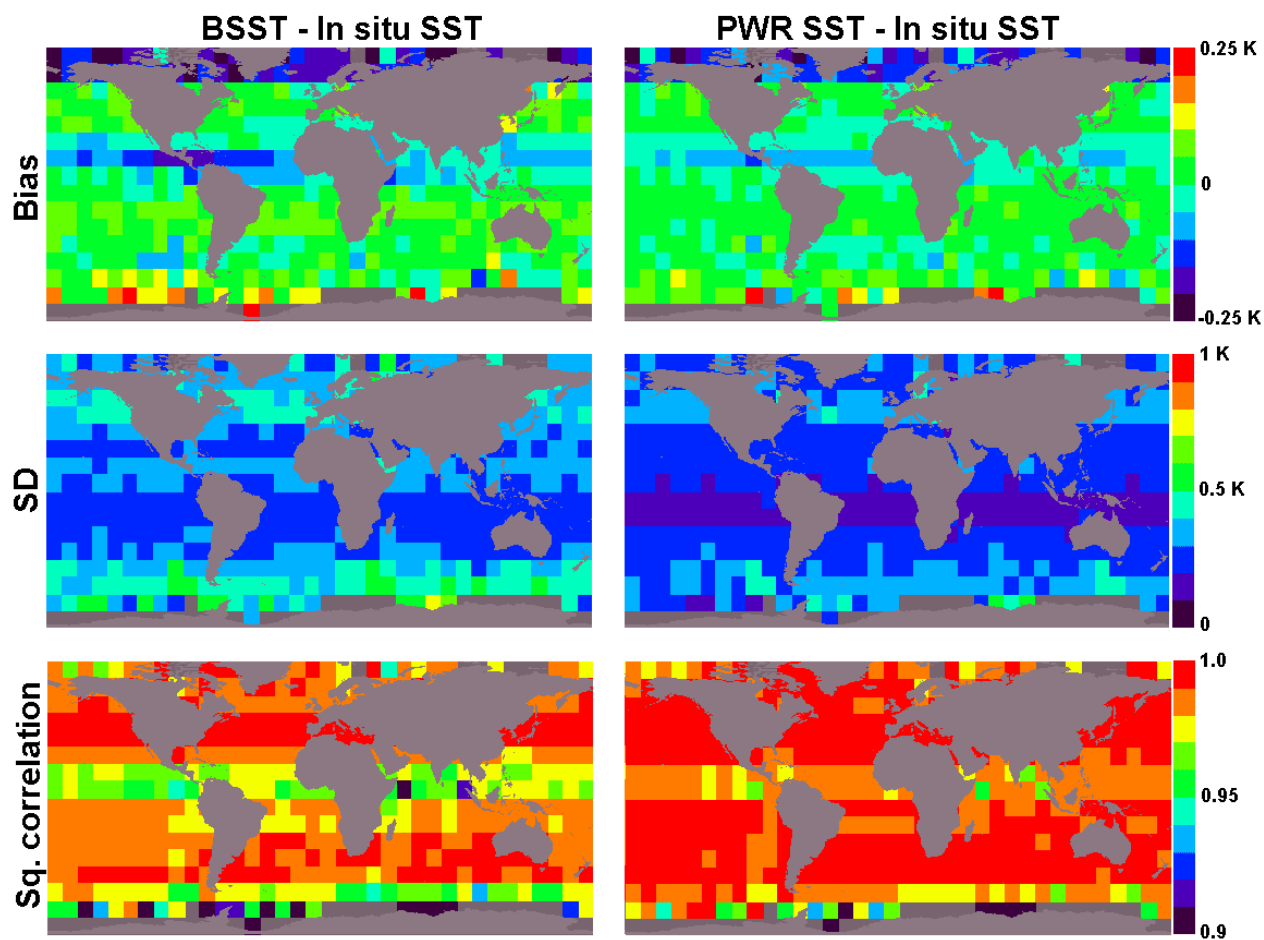


Fig.5. Same as in Fig. 4 but for nighttime.

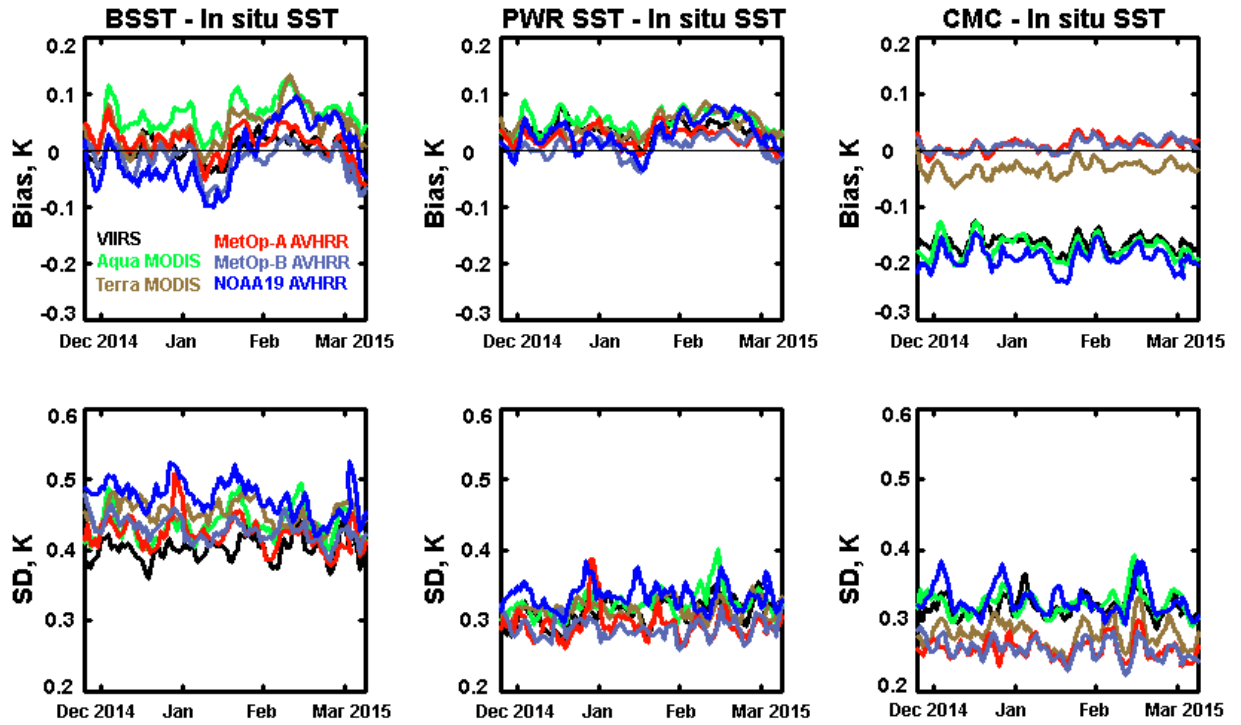


Fig. 6. Time series of daily daytime global biases and SDs of fitting in situ SST with BSST, PWR SST and CMC, for six satellite sensors, from 24 November 2014 to 10 March 2015.

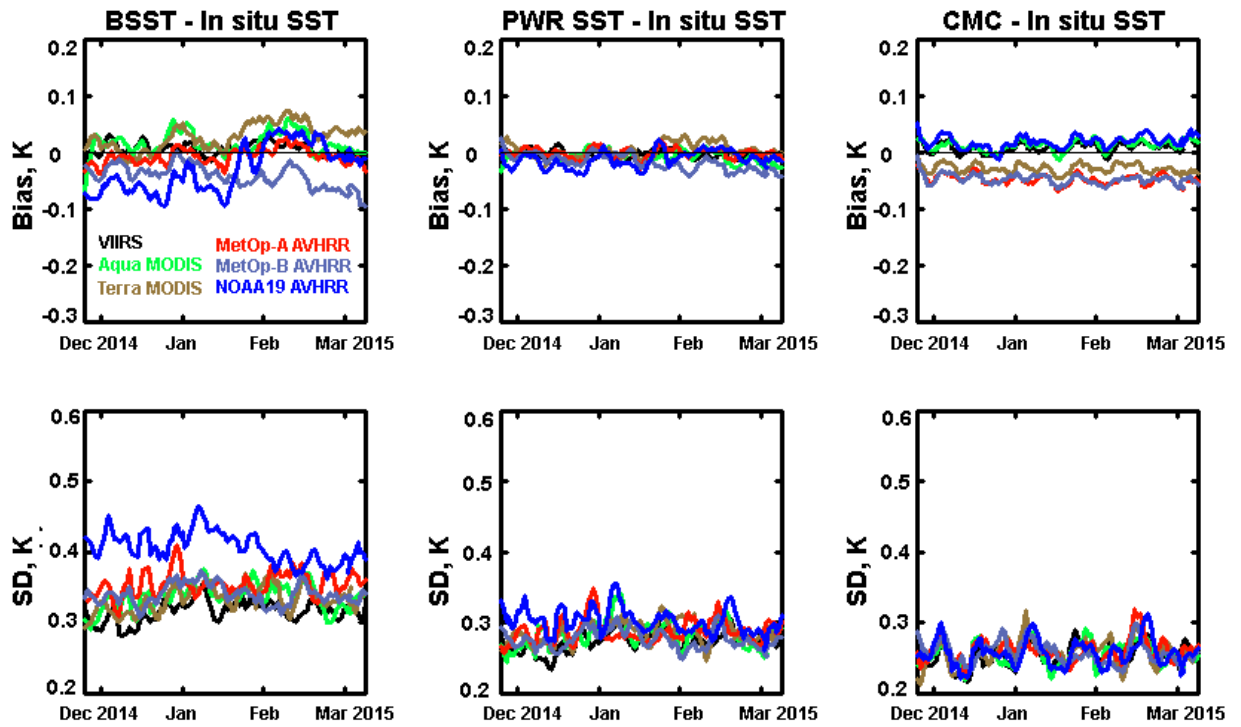


Fig.7. Same as in Fig. 6 but for nighttime.

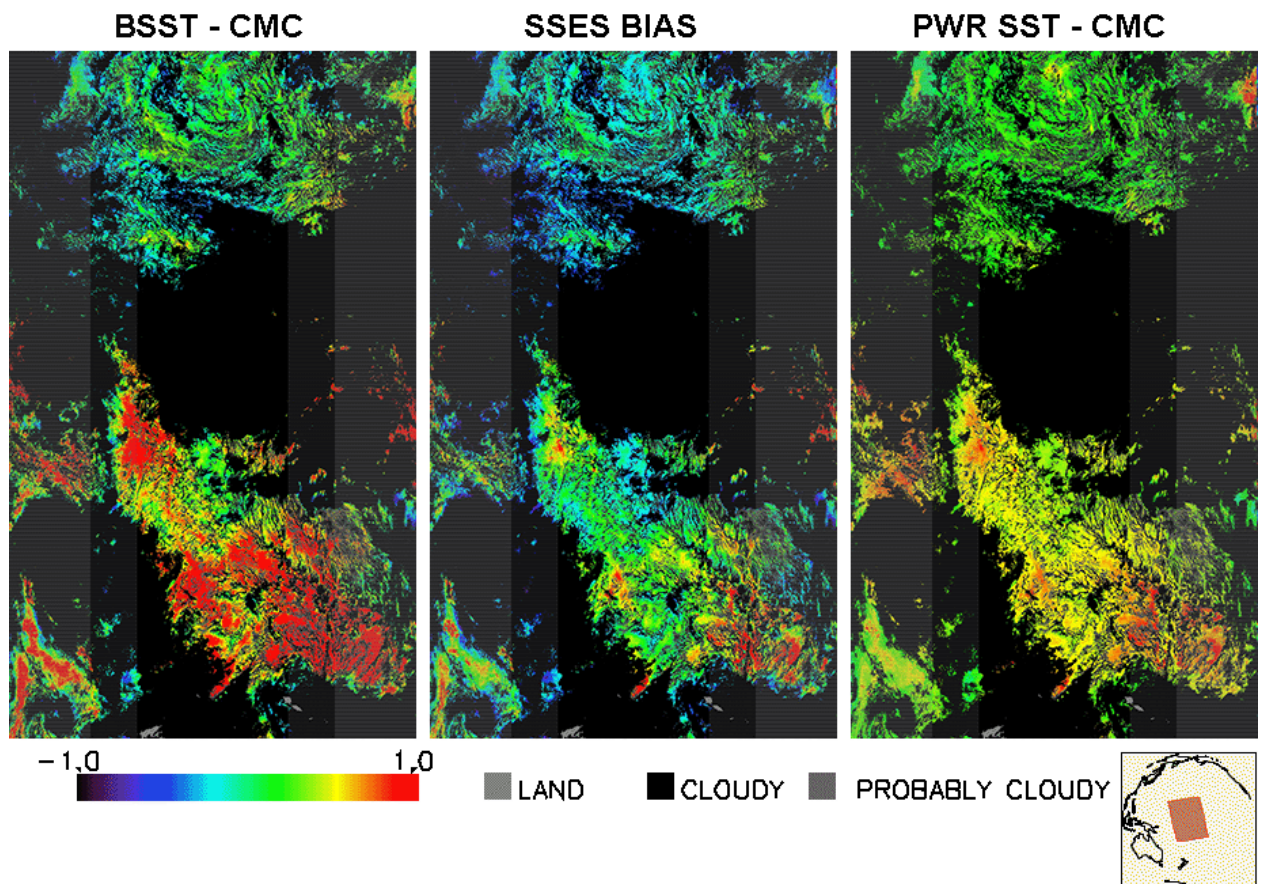
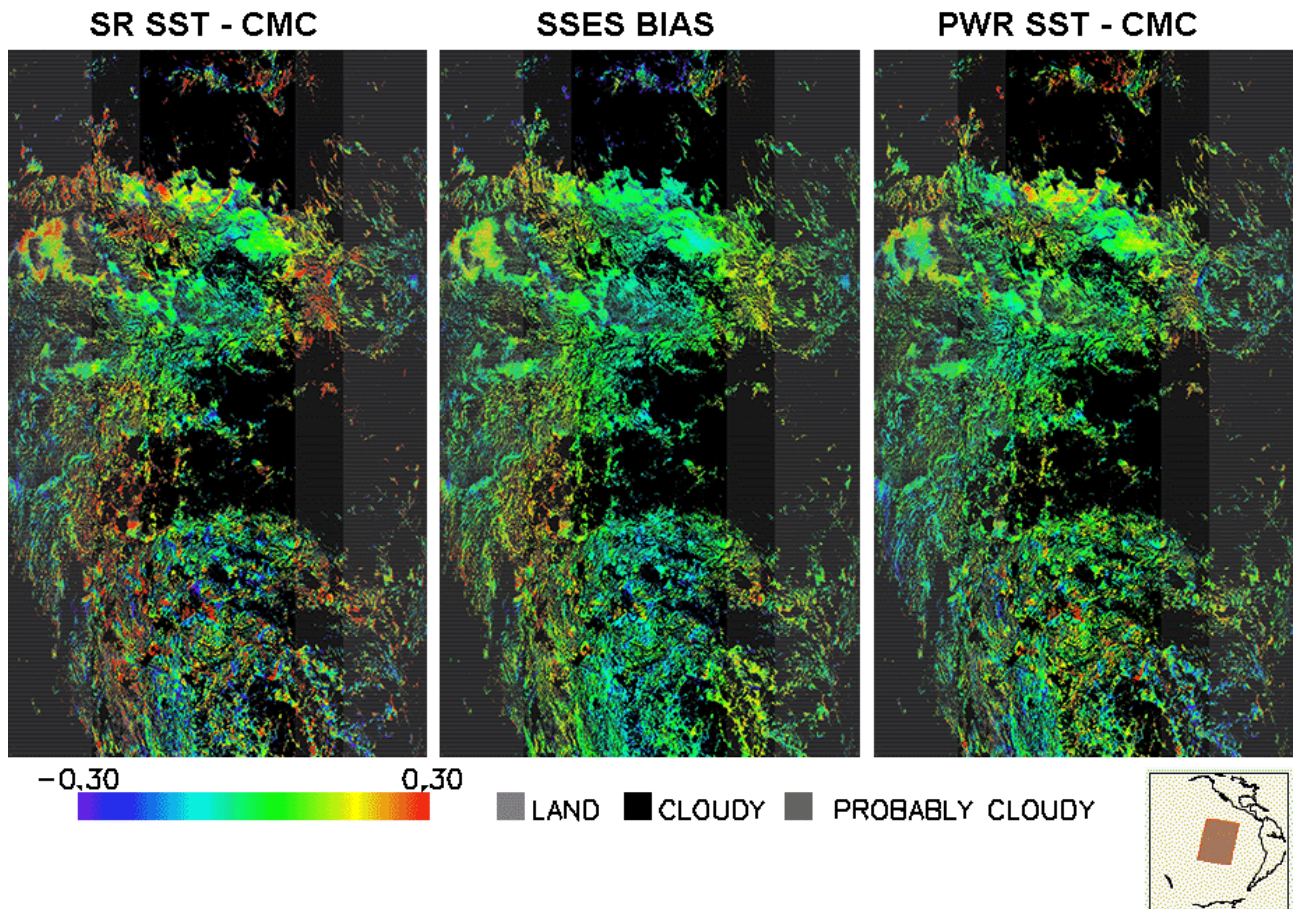


Fig.8. Daytime images of BSST – CMC SST, PWR SST – CMC SST and SSES bias in swath projection from S-NPP VIIRS on 19 December 2014 over the Equatorial Pacific Ocean.





606

607 Fig. 9. Nighttime images of BSST – CMC SST, SSES bias and PWR SST – CMC SST in  
 608 swath projection produced from S-NPP VIIRS observations on 19 December 2014 over the  
 609 Equatorial Pacific Ocean.

610

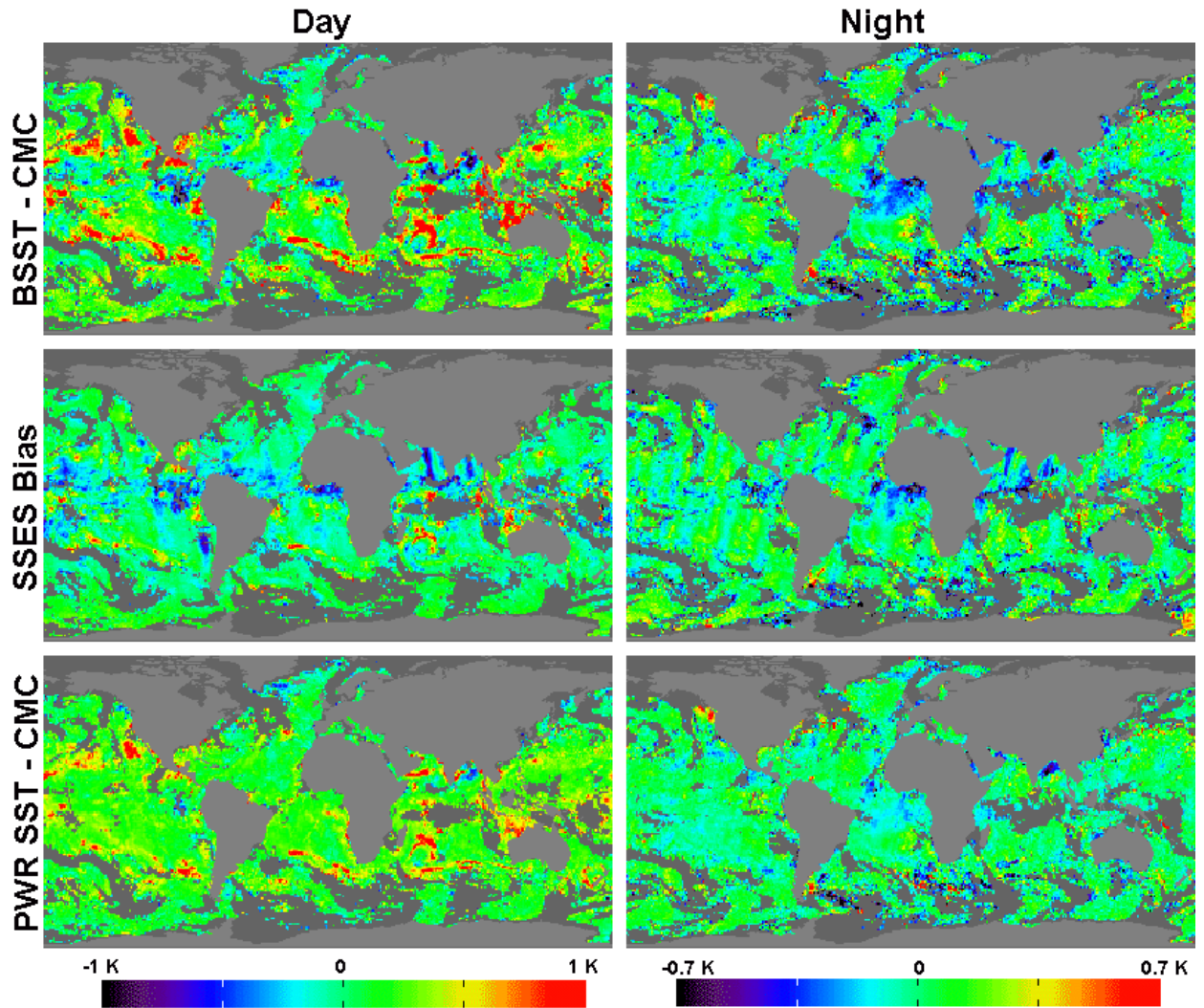


Fig.10. (Left panels) daytime and (right panels) nighttime geographical distributions of (top) BSST-CMC SST, (middle) SSES bias, (bottom) PWR SST- CMC SST from S-NPP VIIRS observations on 16 February 2015.